

Deep Radio Interferometric Imaging with POLISH: DSA-2000 and weak lensing

LIAM CONNOR ,¹ KATHERINE L. BOUMAN ,^{2,1} VIKRAM RAVI ,¹ AND GREGG HALLINAN ¹

¹ Cahill Center for Astronomy and Astrophysics, MC 249-17, California Institute of Technology, Pasadena CA 91125, USA

² Computing and Mathematical Sciences (CMS), Department of Electrical Engineering,, MC 249-17, California Institute of Technology, Pasadena CA 91125, USA

(Received October 17, 2021; Revised October 17, 2021; Accepted)

Submitted to TBD

ABSTRACT

Radio interferometry allows astronomers to probe small spatial scales that are often inaccessible with single-dish instruments. However, recovering the radio sky from an interferometer is an ill-posed deconvolution problem that astronomers have worked on for half a century. More challenging still is achieving resolution below the array's diffraction limit, known as super-resolution imaging. To this end, we have developed a new learning-based approach for radio interferometric imaging, leveraging recent advances in the computer vision problems deconvolution and single-image super-resolution (SISR). We have developed and trained a high dynamic range residual neural network to learn the mapping between the dirty image and the true radio sky. We call this procedure POLISH, in contrast to the traditional CLEAN algorithm. The feed forward nature of learning-based approaches like POLISH is critical for analyzing data from the upcoming Deep Synoptic Array (DSA-2000). We show that POLISH achieves super-resolution, and we demonstrate its ability to deconvolve real observations from the Very Large Array (VLA). Super-resolution on DSA-2000 will allow us to measure the shapes and orientations of $\sim 10^9$ star forming radio galaxies (SFGs), making it a powerful cosmological weak lensing survey and probe of dark energy. We forecast its ability to constrain the lensing power spectrum, finding that it will be comparable and complementary to next-generation optical surveys such as Euclid.

Keywords: methods, machine learning

1. INTRODUCTION

High-resolution imaging of astronomical radio sources plays a critical role in studying our Universe. However, a fundamental challenge of high resolution imaging is that resolution is limited by aperture size (i.e., dish or mirror diameter), rendering single-dish telescopes insufficient in many cases. Alternatively, a radio interferometer is an array of antennas whose radio waves are coherently combined to obtain high resolution images. Radio interferometry allows one to synthesize a much larger aperture, with the angular resolution now defined by the longest “baseline”, i.e. greatest separation, D , between antennas. The diffraction limit of an interferometric array is given by $\theta \approx \lambda/D$, where λ is observing wavelength. Probing scales below this limit is known as “super-resolution”. Interferometry has led to countless new discoveries where single-dish instruments were inadequate, including the first-ever direct image of a black hole ([Event Horizon Telescope Collaboration et al. 2019](#)) and the precise localization of extragalactic transients ([Hallinan et al. 2017; Ravi et al. 2019](#)). The first Nobel Prize in Physics awarded for astronomy was for the development of radio interferometry.

Recovering an image of the sky from an interferometer requires solving an ill-posed deconvolution problem. In particular, the placement of antennas in the interferometer defines a point spread function (PSF) that corrupts the true astronomical image. Preeminent observatories such as the Karl G. Jansky Very Large Array (VLA) and Atacama

Large Millimeter/submillimeter Array (ALMA) have 27 and 66 radio antennas, respectively. In contrast, the upcoming Deep Synoptic Array in the Big Smoky Valley, Nevada, will contain and combine an unprecedented 2000 antennas. The DSA-2000's impressive number of antennas corresponds to a PSF that can be more easily deconvolved, resulting in images with higher fidelity, higher dynamic range, and lower uncertainty. This "radio camera" will be the most powerful radio survey instrument to date and is expected to increase the known sample of astronomical radio sources by a factor of 1000.

The DSA-2000, which will yield unparalleled image quality, will also result in massive computational challenges: the telescope will need to churn through over 80 Tb/s of data. Unlike past radio interferometers that can save data to disk for later analysis, it will be impossible for the DSA-2000 to save raw data to disk. Specifically, the telescope will not preserve its visibility data. It is therefore essential that imaging on DSA-2000 be made fast, automated, and deterministic. Past methods for radio interferometric imaging are either too slow, require a human-in-the-loop, or result in sub-optimal image quality. Thus, it is critical that automated, feed-forward approaches be developed to transform quickly raw dirty images into high-fidelity reconstructions of the radio sky. We capitalize on recent advances in deep learning to develop an imaging pipeline for the DSA-2000 that can be used to deliver science-ready astronomical images in quasi-real time.

It is also essential that DSA-2000 be able to achieve super-resolution. With a PSF width of roughly 3", the majority of the $\sim 10^9$ star forming radio galaxies (SFGs) detected by DSA-2000 will be unresolved or barely resolved in the dirty image. If these distant galaxies can be resolved, we will be able to carry out a powerful cosmological weak lensing survey on DSA-2000. By number of sources, such a survey is competitive with upcoming Stage IV optical weak-lensing experiments. It is also highly complementary because gravitational lensing is achromatic but with different systematics between wavelengths. We therefore have a strong incentive to not only develop a robust feed-forward imaging framework, but one that provides super-resolution.

In this work, we demonstrate that recent advances in the classical problems of single-image super-resolution (SISR) and deconvolution through efficient neural network architectures make such imaging with the DSA-2000 possible. This manuscript is organized as follows. We first offer background on interferometric imaging, the DSA-2000, and the connection to SISR and deconvolution in Section 2. We then describe our deep learning based approach in Section 3, which we call POLISH. As we show, POLISH enables imaging at angular resolutions on the sky below the intrinsic resolution of the interferometric telescope array (≈ 3 arcseconds for DSA-2000). Results based on simulated DSA-2000 data as well as on real astronomical data from the VLA are presented in Section 4. In Section 5, we show how super-resolution on DSA-2000 will enable a powerful weak lensing survey. Finally, we discuss other scientific applications and show how feed-forward imaging could transform radio astronomy in coming years.

2. BACKGROUND

2.1. Interferometric imaging

In radio interferometry, each pair of antennas measures a Fourier coefficient of the underlying astronomical image, where the spatial frequency probed is related to the projected baseline between the antennas as well as the observing wavelength. Imaging then requires solving an inverse problem: recover the true sky image, I_{sky} , using finite, and often sparse, spatial frequency measurements. Given enough antennas, one could densely sample the entire spatial frequency plane. In the absence of noise, these complex measurements, known as "visibilities" V , could then be used to recover an image through an inverse Fourier transform:

$$I_{\text{sky}} = \mathcal{F}^{-1}(V). \quad (1)$$

Since we only have access to a finite number of spatial frequency Fourier coefficients in practice (i.e. a finite number of antennas pairs and finite range of radio frequencies), we do not have full access to V . We mathematically represent this by applying a sampling function, S , to the noisy measurements in the Fourier plane,

$$I_{\text{d}} = \mathcal{F}^{-1}((V + n_{\text{vis}})S), \quad (2)$$

where n_{vis} represents independent Gaussian noise at each spatial frequency. Invoking the convolution theorem, we can rewrite this equation as

$$I_{\text{d}} = \mathcal{F}^{-1}(V) \otimes \mathcal{F}^{-1}(S) + n_{\text{sky}}, \quad (3)$$

where $n_{\text{sky}} = \mathcal{F}^{-1}(n_{\text{vis}}) \otimes \mathcal{F}^{-1}(S)$. The inverse Fourier transform of the sampled visibilities, I_{d} , is known as the "dirty image". By noting that the Fourier transform of our sampling function is just the instrument's PSF, we can replace

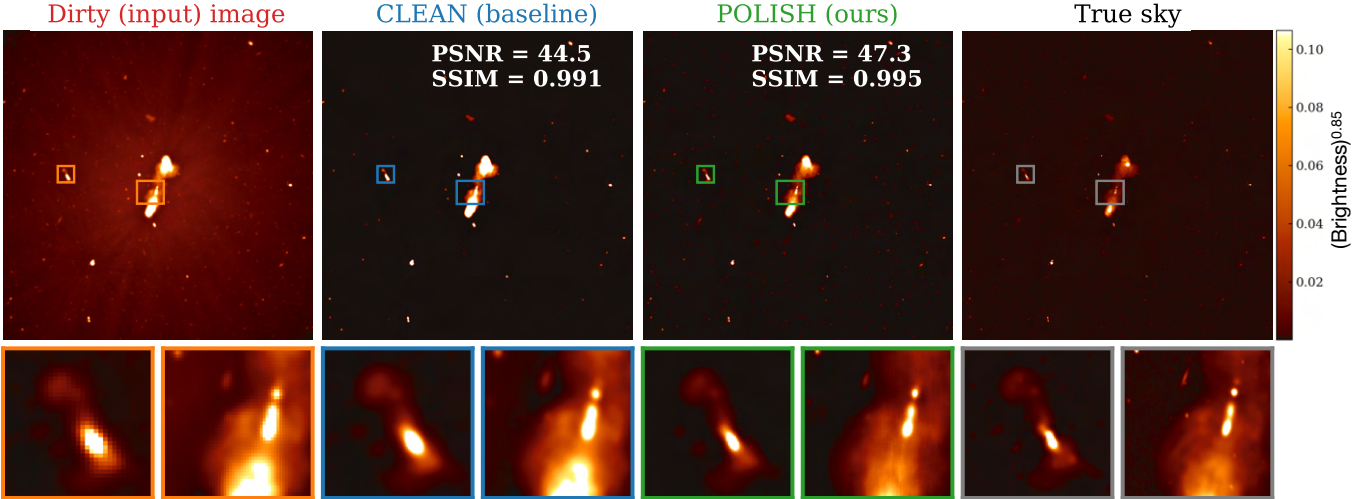


Figure 1. We propose a learning-based approach to recover a super-resolved astronomical image from a “dirty” input image captured by a radio interferometer. Our method, “POLISH” (green), significantly outperforms the image-plane CLEAN algorithm (blue) on realistic simulations of radio images. Training data was significantly different from the radio sky image used in this example (training images were composed entirely of simple elliptical Gaussian shapes; see Section 4.1), but POLISH is still able to recover structured sources in the image. POLISH resolves finer spatial structures and achieves higher PSNR and SSIM than CLEAN. Data are normalized between 0 and 1 then raised to the power of 0.85 to better visualize faint structures. Each image is 0.26×0.26 degrees.

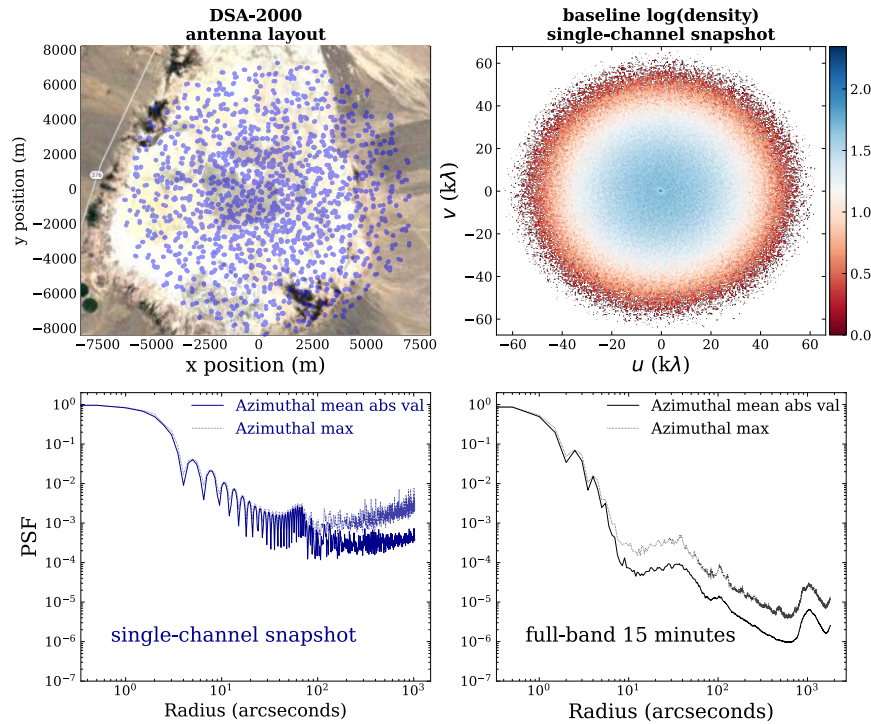


Figure 2. For our primary training set, we used the DSA-2000 layout shown here. The top left panel shows antenna position assumed for our simulation overlaid on Big Smoky Valley, Nevada. The top right panel shows the array’s UV coverage for a single frequency at a single time, represented as the logarithm of baseline density. The bottom two panels show an azimuthal average and maximum of the absolute value PSF for a single-channel snapshot (left) and the full band 15-minute integration (right). We expect the DSA-2000 layout to be further optimized for sidelobe suppression and azimuthal smoothness before it is built.

$\mathcal{F}^{-1}(S)$ with a convolution kernel k . This kernel depends not only on the telescope configuration but also the radio bandwidth, as can be seen in Figure 4. Finally, we are free to choose a pixelization scheme such that the resolution of the recovered image, \hat{I}_{sky} , is s times higher resolution than I_{d} . By substituting Eq. 1, we obtain a mathematical description of the noisy and low-resolution image obtained by the interferometer, I_{d} , as a function of our target, I_{sky} :

$$I_{\text{d}} = (I_{\text{sky}} \otimes k) \downarrow_s + n_{\text{sky}}. \quad (4)$$

The goal of our work is to learn this mapping such that Eq. 4 can be inverted and an estimate for the true sky, \hat{I}_{sky} , can be automatically recovered with a single pass through a neural network.

2.2. The Deep Synoptic Array (DSA-2000)

The Deep Synoptic Array, i.e., DSA-2000, is an ambitious new instrument expected to be complete by 2026 (Hallinan et al. 2021). It will survey the radio universe with unprecedented speed and depth, but this power comes at the expense of serious computational challenges. The DSA-2000 will consist of 2000×5 m dual-polarization antennas observing the sky between 0.7 and 2.0 GHz. By the Nyquist–Shannon sampling theorem, the DSA-2000 must sample the electric field at more than 4 billion times per second, resulting in a raw data rate of over 80 Tb/s. At the next stage in the pipeline, a single image of the sky produced using 15-minutes of visibility measurements requires ≈ 20 TB of data. This tremendous data rate prevents the use of imaging algorithms that store data and iteratively transform from visibilities in the Fourier plane to images in the sky plane. Instead, computational resources require that the DSA-2000 imaging pipeline rapidly recover an image of I_{sky} from I_{d} directly. In our proposed method, POLISH, we have developed a feed forward approach to invert a $2,000 \times 2,000$ pixel image, I_{d} , into a sky reconstruction in just a few seconds on a laptop.

2.3. Prior interferometric imaging techniques

Over the past half-century, considerable effort has been put into radio interferometric image reconstruction. While significant progress has been made, state-of-the-art algorithms do not satisfy the requirements for efficient super-resolution imaging on the DSA-2000. Imaging algorithms can be broadly categorized into two methodologies: CLEAN deconvolution and regularized maximum likelihood (RML) approaches.

CLEAN The de facto standard image reconstruction algorithm used in radio astronomy is known as CLEAN (Högbom 1974; Clark 1980). CLEAN attempts to iteratively deconvolve the PSF kernel k from I_{d} to recover I_{sky} , by assuming the sky is made up of a collection of point-sources. At each step, single pixels are added to a sky model at the locations of bright pixels in I_{d} . The model pixels are scaled by the brightness of the corresponding pixels in I_{d} . The sky model is then convolved with a Gaussian “restoring beam” to provide a smooth estimate of the recovered image. This final blurring step, necessitated by the point-source assumption in CLEAN, precludes CLEAN from recovering high spatial frequencies. This is because the restoring beam smooths data to the angular scale of the central component of the PSF. Besides not being able to deliver super-resolution, standard iterative algorithms like CLEAN introduce severe imaging artifacts near very bright or diffuse radio sources.

Regularized Maximum Likelihood Regularized Maximum Likelihood (RML) methods are Bayesian inspired techniques that solve for an image by minimizing an objective function, which includes a term that penalizes poor data fit and an image regularization term (Wiaux et al. 2009; Bouman et al. 2016; Sun & Bouman 2020). Some image regularization terms employed include maximum entropy (Narayan & Nityananda 1986), total variation, and ℓ_1 sparsity (Pratley et al. 2018). RML methods have had recent success in the radio interferometry community in their use for reconstructing the first image of a black hole, M87* (Akiyama et al. 2019). Since RML methods do not rely on the CLEAN assumption that the sky is composed of point-sources, they can achieve super-resolution (Abdulaziz et al. 2019). However, they are very computationally expensive since they are iterative and model every measurement in the visibility domain. Though RML methods provide a more natural way of achieving super-resolution than CLEAN, these algorithms are not well suited for the DSA-2000 where fast, feed-forward image reconstruction is essential.

2.4. Deconvolution & single image super-resolution

Deconvolution is a classic inverse problem that aims to reconstruct a sharp image by removing an imaging system’s PSF from its measured blurry image (Riad 1986; Starck et al. 2002). Traditional approaches to deconvolution include Weiner filtering and regularized inversion, however recently deep learning approaches have demonstrated impressive results on the task (Xu et al. 2014; Yan & Shao 2016). Single Image super-resolution (SISR) is an ill-posed inverse

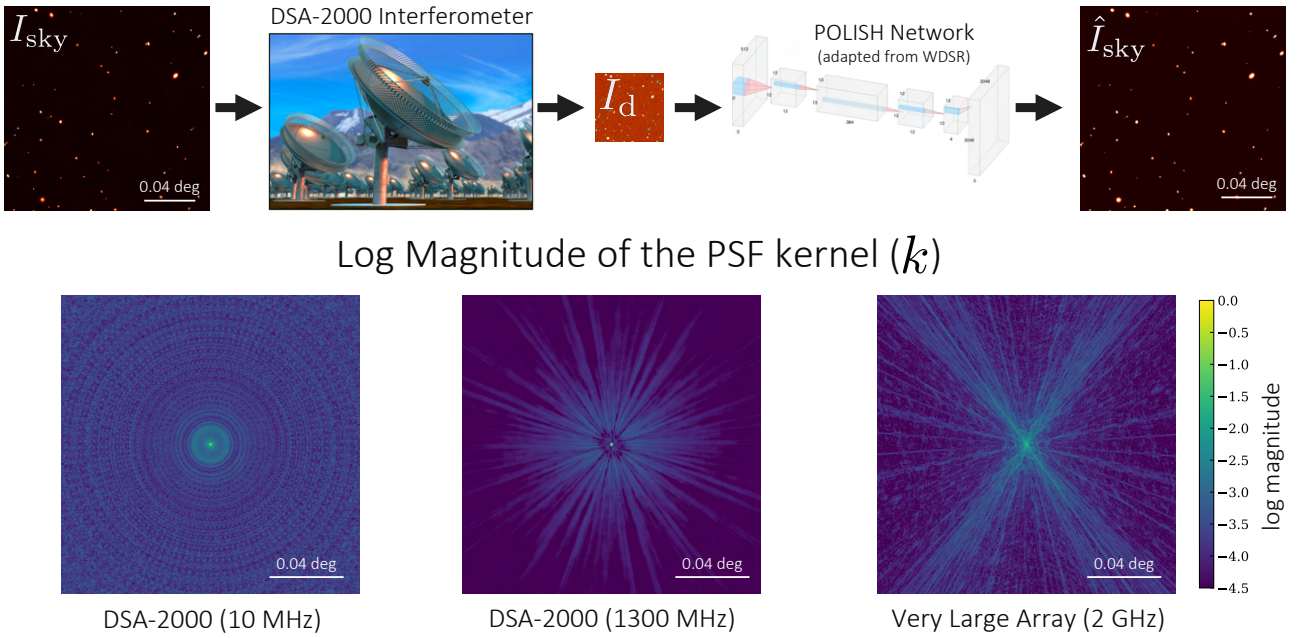


Figure 3. A schematic of the POLISH method of image reconstruction. The top row shows how the true sky is transformed by a radio interferometer and then recovered by our neural network. The bottom three figures show the PSF kernels used in this work: the DSA-2000 with just 10 MHz of its bandwidth used (left), and the full-band (1300 MHz) PSF of the DSA-2000 (middle), and an example VLA array configuration (right). Note that these kernels are plotted over the same extents as the observed sky images, highlighting that the kernels cause artifacts from bright sources that extend over the entire images.

problem in which one attempts to obtain a high-resolution (HR) output from its corresponding low-resolution (LR) image (Glasner et al. 2009; Yang et al. 2014). Here too, deep learning based approaches to SISR have made significant progress, and efficient neural network architectures continue to be developed to learn the mapping between the high- and low-resolution images (Dong et al. 2015; Ledig et al. 2017; Yang et al. 2019). SISR shares conceptual similarities with deconvolution, since one can frame the SISR problem as removing the downsampling operation’s PSF from the image. However, unlike deconvolution, the mismatch in dimensions between the desired HR and input LR image causes the inverse problem to be ill-posed. The challenge of image reconstruction in radio interferometry can be formulated as a joint deconvolution and SISR inverse problem. In fact, replacing I_d/I_{sky} with $I_{\text{LR}}/I_{\text{HR}}$ in Eq. 4 reproduces the generalized SISR image degradation equation used in (Yang et al. 2019).

There are nonetheless four critical differences between standard deconvolution-SSIR and astronomical imaging with radio interferometers. First, images of the radio sky require large dynamic ranges. In the annual New Trends in Image Restoration and Enhancement (NTIRE) data challenge for SISR, the image pairs were RGB 8-bit precision and roughly $2,000 \times 2,000$ pixels. In contrast, a typical 1 deg^2 field on the sky measured with the DSA-2000 radio interferometer will have $\sim 20,000$ unique sources with a range of brightness values approaching five orders of magnitude. Thus, we require at least 16-bit integers or preferably, 32-bit floats. Second, both the sky and instrument response are dependent on observing frequency. We therefore prefer multifrequency input data with an arbitrary number of channels, a generalization of the three color channels used for RGB images. Third, the PSF in radio astronomy can be highly spatially extended, unlike the simple Gaussian blurring kernel or bi-cubic downsampling typically assumed in many super-resolution applications. The PSF can also have significant radial and azimuthal structure (refer to Fig. 4). Fourth, while the response of our instrument is knowable in principle, calibration errors and other systematics lead to perturbations of the PSF. Therefore, our neural network must learn not just a single kernel, but a physically realistic distribution of PSFs (akin to partially blind deconvolution).

3. METHODS

We modify the previously proposed Wide Activation for Efficient and Accurate Image Super-Resolution (WDSR) (Yu et al. 2018) architecture to allow for high-dynamic range and multifrequency input/output data, as well as to

handle uncertainty in the PSF. This architecture is shown in Fig. 4.¹ Our adaptation, POLISH, takes as input a dirty image, I_d : a tensor with dimension (n_x, n_y, n_f) where n_f is the number of frequency channels. POLISH outputs a super-resolved reconstruction of the sky, \hat{I}_{sky} , whose shape is $(s n_x, s n_y, n_f)$. Here, s is the upsampling factor and takes values 2 or 3 in our work. The architecture depends on a residual network design with a single global skip connection and a residual block called “WDSR_b”. The final operation before the global skip connection and the primary path are summed is known as a pixel shuffle. These layers upsample the image by a factor of s , using a sub-pixel convolution with stride $1/s$ (Shi et al. 2016). To ensure high dynamic range deconvolution, POLISH now accepts as input 16-bit, or 32-bit data.

We train the POLISH network, G_θ , on N image pairs $(I_d^{(n)}, I_{\text{sky}}^{(n)})$, related through Eq. 4, to minimize an ℓ_1 loss:

$$\hat{\theta} = \arg \min_{\theta} \sum_n \left\| I_{\text{sky}}^{(n)} - G_\theta(I_d^{(n)}) \right\|_1 \quad (5)$$

The model is trained with roughly 10^6 total epochs and a constantly decaying learning rate between 10^{-3} to 5×10^{-4} . After each 1000 epochs of training, the model is tested on 10 images from the validation set, and a checkpoint is saved if its PSNR has improved. For results presented in this main paper, we use 800 image pairs for our training data and 100 pairs in our validation set. Each model takes roughly 20 GPU hours to train using an NVIDIA TITAN RTX GPU with 24 GB of memory². Before PSNR is calculated, or an I_d is fed to POLISH, data are normalized such that the image’s pixel values fall between 0 and $2^{n_{\text{bit}}} - 1$.

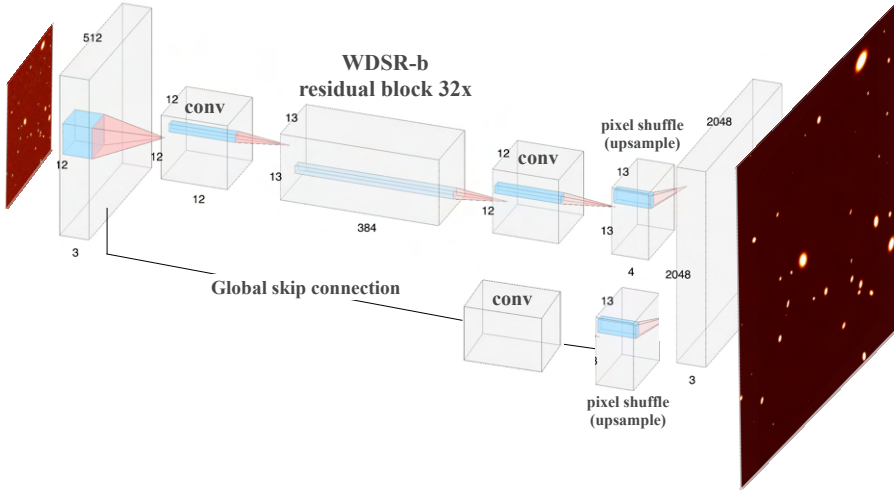


Figure 4. The neural network architecture that we have adapted for radio imaging, based on WDSR (Yu et al. 2018). A dirty image is fed to the network as an input and its output is a deconvolved reconstruction of the sky with s times greater resolution in each direction. The network relies on residual blocks and a global skip connection. Batch normalization is removed.

3.1. Learning a PSF distribution

In radio interferometry an idealized PSF kernel is known *a priori*, as it is simply the inverse Fourier transform of the sampling function, $k_{\text{ideal}} = \mathcal{F}^{-1}(S)$. However, in practice the instrumental response will cause the PSF to deviate from the ideal model due to, e.g., calibration errors. We therefore want the POLISH network to learn a distribution of PSFs, rather than a single PSF kernel. We build this into our training set by randomly perturbing the PSF in physically motivated ways when generating training image pairs. In particular, for each training pair the dirty image is created by applying a kernel that has been transformed in the following way,

$$k = \Lambda_3(\phi)\Lambda_2(\gamma)\Lambda_1(\alpha) k_{\text{ideal}}. \quad (6)$$

¹ We based our implementation on the publicly available code at <https://github.com/krasserm/super-resolution> under the Apache License 2.0 license.

² Training was done on an internal cluster. The total compute spent on this project was roughly 300 GPU hours.

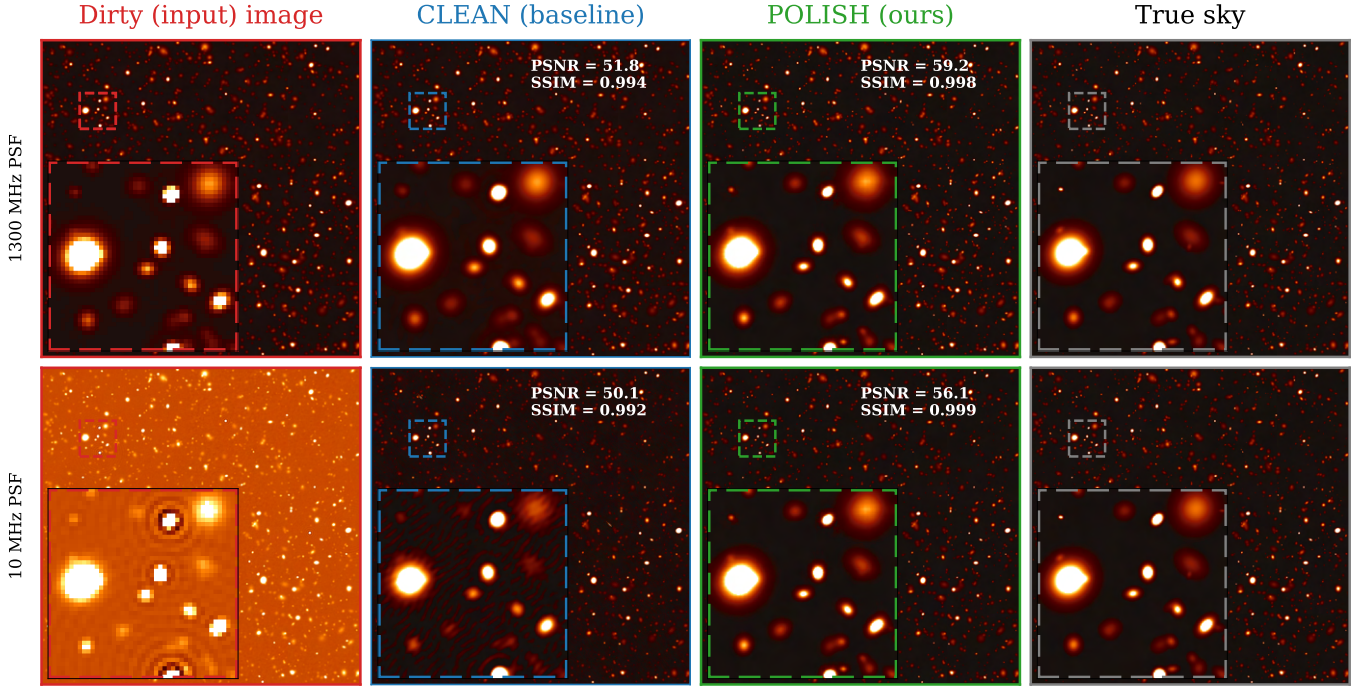


Figure 5. A simulated DSA-2000 interferometric observation of distant radio galaxies and the image reconstruction by CLEAN (middle left) and POLISH (middle right). The bottom row shows the sky convolved with DSA-2000’s PSF using less than 1% (single-channel snapshot); this case is critical for HI and OH science. The top row PSF uses the full-band with 15-minutes of integration and has a more complete sampling in the Fourier plane. In both cases POLISH outperforms the image-plane CLEAN baseline, especially for the 10 MHz PSF where substantial artifacts exist in the CLEAN reconstruction. The brightness of each image is independently scaled for visualization purposes.

These three transformations include a radial stretch, $\Lambda_1(\alpha) : r \rightarrow \alpha r$ where the PSF shape is conserved but its size varies by tens of percent; this degradation is motivated by ionospheric effects that broaden the kernel but never shrinks it (i.e., α is drawn from $(0,1]$). $\Lambda_2(\gamma)$ warps the PSF with random distortions, characterized by a parameter γ , as seen in Fig 7. Finally, an affine transformation $\Lambda_3(\phi)$ both contorts the PSF and shifts it with a spatial translation, similar to what occurs when a telescope is mispointed.

3.2. Loss function and performance metric

We have tried training our model using L^1 and L^2 loss functions. Both are pixel-wise loss functions that measure the mean absolute error and mean squared error between input and output images, respectively. We find that the L^1 loss gives better results, in line with previous EDSR and WDSR networks (Lim et al. 2017; Yu et al. 2018). The final results presented here were trained using L^1 loss.

As a way of assessing the veracity of our reconstructed image and the performance of our neural network, we use two metrics. The first is peak signal-to-noise ratio (*PSNR*), which a standard statistic used in computer vision. PSNR is a pixel-by-pixel estimator of the ratio of maximum signal and corrupting image noise, expressed in decibels. It is given by,

$$PSNR = 20 \log \left(\frac{MAX_I}{MSE} \right), \quad (7)$$

where MAX_I is the maximum possible pixel value in an image, and MSE is the mean squared error across all pixels. For an 8-bit RGB image, MAX_I is 255. In general, it is $2^{N_b} - 1$ where N_b is the number of bits per sample. The MSE is calculated as the average square difference between the true image and the reconstructed, given by,

$$MSE = \frac{1}{N_l N_m} \sum_l \sum_m (I_{\text{sky}}(l, m) - I_{\text{SR}}(l, m))^2. \quad (8)$$

$PSNR$ depends on pixel-wise error, making it sensitive to translations of the image, or “astrometric error” in our case. Since we are concerned here with small distortions to galaxy shapes, we also employ a more perception-based metric known as the structural similarity index measure ($SSIM$)³ (Wang et al. 2004). $SSIM$ compares small windows within an image to assess the statistics of those regions, rather than directly computing absolute differences in pixels. We use both $SSIM$ and $PSNR$ to test the performance of POLISH.

4. EXPERIMENTAL SETUP & RESULTS

The performance of POLISH is assessed on both realistic simulations mimicking data from the DSA-2000, as well as real experimental data from the VLA at 2–4 GHz. We compare the POLISH reconstruction with image-plane CLEAN and the true image (in the case of simulated sky data), using both PSNR and SSIM to quantify reconstruction quality.

4.1. Synthetic training data

We model the radio sky and measurement noise to simulate a physically realistic training set. This is done by first simulating a $\sim 2,000 \times 2,000$ pixel image of the true sky, I_{sky} with a field of view of $\sim 0.3 \times 0.3$ deg. DSA-2000 will primarily detect radio galaxies in the distant Universe with a detection rate corresponding to an average of 13,000 galaxies per square degree above a signal-to-noise (SNR) of 6 (Hallinan et al. 2021). We populate each realization of I_{sky} with N sources, where N is randomly drawn from a Poisson distribution whose mean is 13,000 times the sky coverage in degrees. The galaxies are 2D Gaussian ellipsoids with random orientation angles on the sky. The statistics of their brightness, ellipticity, and angular size are chosen to match the empirically measured distributions for radio galaxies (Tunbridge et al. 2016). The range of galaxy peak flux values range from a few to several thousand microJanskys/pixel. We describe the simulation in greater detail in Appendix A.

A dirty image, I_d , corresponding to each true sky image is obtained through the process mathematically described in Eq. 4. The PSF kernel used to degrade I_{sky} is obtained by sampling from Eq. 6. The unperturbed PSF is computed for each telescope configuration using the packages `casa` (McMullin et al. 2007) and `wsclean` (Offringa et al. 2014). Before applying the PSF kernel to obtain I_d , zero-mean *i.i.d.* Gaussian noise with a standard deviation σ_{sky} is applied to mimic n_{sky} . The convolved image is then downsampled by a factor s . The parameters $\sigma_{\text{sky}} = 0.5$ microJanskys/pixel and $s = 3$ are used to simulate DSA-2000 dirty images, while values of $\sigma_{\text{sky}} = 3$ microJanskys/pixel and $s = 2$ are used for generating VLA training data used in Section 4.2.3.

Results presented in the main paper consist of 16-bit single-channel input data, where a multifrequency dependence has been included in the PSF kernel but not I_{sky} . On DSA-2000, we use two PSFs: one that uses the full radio bandwidth (1300 MHz) with 15 minutes of earth-rotation synthesis and one that uses just $\sim 1\%$ of the observing bandwidth (a narrow 10 MHz range of wavelengths) for a single snapshot, shown in Fig. 3. If the PSF is generated across multiple frequencies, it is effectively averaged over the band to produce a single channel.

4.2. Results

Figure 1 visually compares the performance of POLISH against the baseline CLEAN algorithm on synthetic DSA-2000 observations, using an SKA Data Challenge image as I_{sky} (Bonaldi et al. 2021). The input dirty image, corresponding to a 1300 MHz bandwidth PSF, is shown on the left. Although POLISH was only trained on images with Gaussian sources, it is able to recover more complex underlying sharp structure. As demonstrated by the increase in PSNR and SSIM, POLISH recovers a substantially improved image compared to both the measured dirty image and the CLEAN reconstruction, at nearly 3 dB higher than the latter.

Figure 5 shows a visual example of POLISH results on DSA-2000 synthetic data, comparing results on data generated with a 10 MHz and 1300 MHz bandwidth PSF. In order to best see the improvement, each panel shows a zoom-in on a $0.06 \text{ deg} \times 0.06 \text{ deg}$ region of the full simulated sky, where dozens of radio galaxies with different sizes, shapes, and orientations can be seen. In the 10 MHz bandwidth PSF, less than 1% of the available radio wavelengths are used to construct the PSF; reconstructing an image with only a small portion of the full PSF bandwidth is important for HI and OH studies on DSA-2000. This region of the sky has two particularly bright “galaxies”, which makes the PSF visible in the 10 MHz bandwidth dirty image.

In both cases POLISH substantially outperforms the CLEAN baseline. POLISH achieves a mean $PSNR=55.9 \pm 4.7$ and $SSIM=0.998 \pm 0.0016$ for our radio galaxy simulation with the 1300 MHz PSF on 50 validation images, com-

³ https://en.wikipedia.org/wiki/Structural_similarity

Bandwidth (MHz)	PSNR (POLISH)	PSNR (CLEAN)	SSIM POLISH	SSIM CLEAN
1300	55.9 ± 4.7	50.0 ± 6.0	0.998 ± 0.0016	0.989 ± 0.007
10	55.1 ± 3.8	47.4 ± 3.6	0.988 ± 0.0016	0.976 ± 0.009

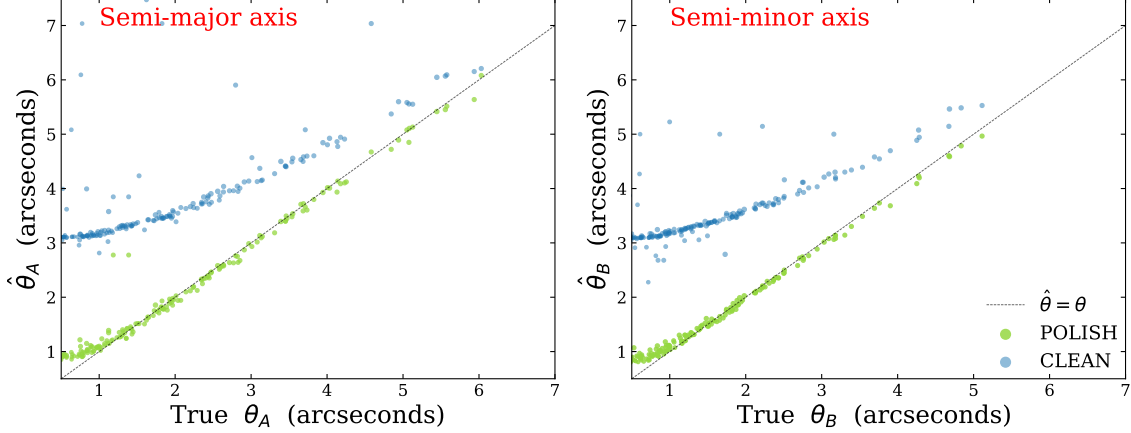


Figure 6. A comparison of the resolving power of POLISH (green dots) with that of traditional CLEAN algorithm (blue dots) on simulated DSA-2000 data with a 1300 MHz PSF kernel. The vertical axes are the fitted semi-major (left) and semi-minor (right) axes, $\hat{\theta}$, of hundreds of “galaxies” in the reconstructed images. They are plotted against the true galaxy sizes in arcseconds. CLEAN’s resolving power asymptotes to the PSF angular scale preventing it from achieving super-resolution, while POLISH achieves accurate super-resolution well below the intrinsic resolution of the interferometer (≈ 3 arcseconds). Note that we find **Source-Extractor** slightly underestimates both θ and $\hat{\theta}$ along both the major and minor axes in all images.

pared with $\text{PSNR}=50.0 \pm 6.0$ and $\text{SSIM}=0.989 \pm 0.007$ on CLEAN.⁴ The 10 MHz PSF results in $\text{PSNR}=55.1 \pm 3.8$ and $\text{SSIM}=0.988 \pm 0.0016$ using POLISH. For CLEAN this was $\text{PSNR}=47.4 \pm 3.6$ and $\text{SSIM}=0.976 \pm 0.009$.

4.2.1. Super-resolution

Super-resolution is critical for many scientific goals of the DSA-2000. We therefore investigate if spatial scales below the width of the PSF’s central lobe (≈ 3 arcseconds) can be reliably accessed with POLISH. We quantify the super-resolution capability of POLISH using the galaxy simulations described in Section 4.1. First, the size of each “galaxy” is extracted using the astronomical fitting software **Source-Extractor** (Bertin & Arnouts 1996). This is done on the true image, CLEAN image, and the POLISH image. The fitted galaxy sizes are then compared on a source-by-source basis; for each galaxy, we contrast the input (true sky) and output (POLISH and CLEAN reconstructions) semi-major (θ_A) and semi-minor axes (θ_B). If the reconstructed value, $\hat{\theta}$, is below the PSF angular scale of ≈ 3 arcseconds, then super-resolution has been achieved. As can be seen in Fig. 6, galaxies in the POLISH image are consistently the same size as galaxies in the true image, even at sub-arcsecond scales well below the DSA-2000’s PSF size. In contrast, the traditional CLEAN algorithm cannot achieve super-resolution and instead asymptotes to the PSF central component’s angular size.

4.2.2. Model mismatch

When a distribution of PSFs are used during training, POLISH can more robustly reconstruct the sky in the presence of instrumental calibration errors. In the supplemental material we perform an ablation study showing how performance decreases when training data is restricted to images corrupted with the ideal PSF kernel k_{ideal} .

In Fig. 7 we demonstrate POLISH image reconstruction on test data whose PSF has been perturbed outside of the range of training data perturbations. In particular, POLISH has been trained with PSF kernels transformed by the warp function $\Lambda_2(\gamma)$ described in Section 3.1, with γ drawn from a uniform distribution between 0 and 20. The training data PSFs were not radially stretched for this figure, allowing us to test POLISH’s performance under model

⁴ The number of validation images was limited by CLEAN computational requirements.

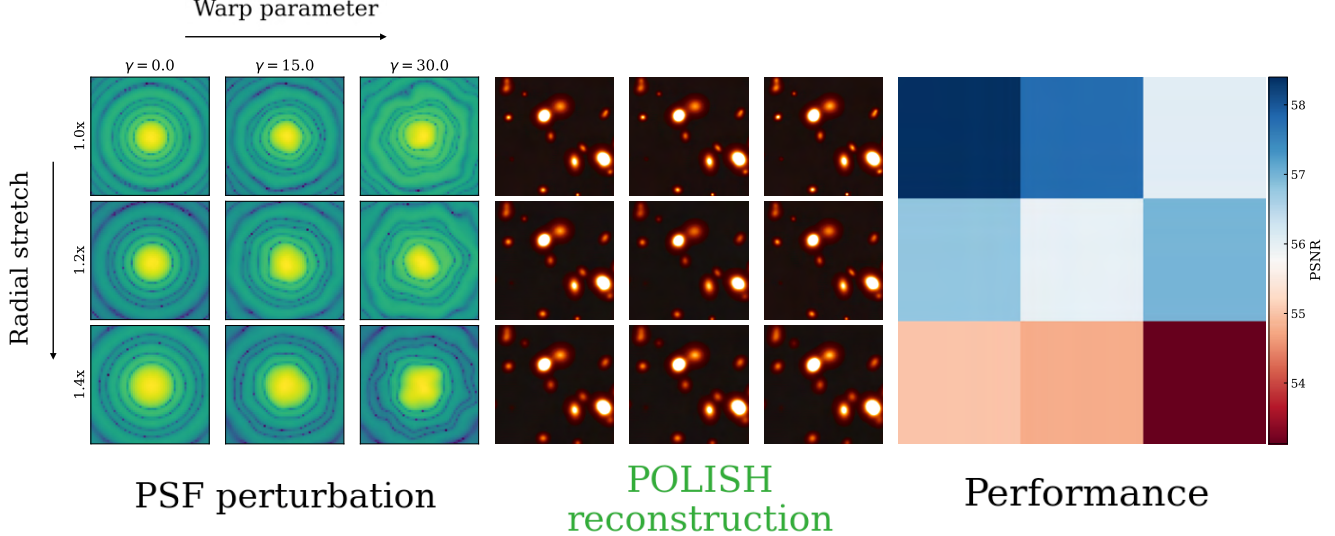


Figure 7. The impact of model mismatch on reconstruction performance. POLISH has been trained using a distribution of PSF kernels with warps in the range of $\gamma=0$ to 20. We then validate on dirty images that have been corrupted by a PSF kernel that has been radially stretched (increasing downwards) and warped (increasing to the right), the logarithm of which is shown on the left (zoomed in on the PSF’s inner 28×28 arcseconds). The corresponding POLISH images and PSNRs are shown in the middle and right, respectively.

mismatch. As can be seen in the PSNR performance plot, the quality of the recovered test images degrades as the PSF perturbations get larger than the training set distortions. However, even in the relatively extreme distortions (bottom right element of each 3×3 grid) PSNR remains above 50 (and comparable to or better than the typical CLEAN-based PSNRs above). Such distortions and uncertainty in the DSA-2000 PSF are greater than what we expect for actual experimental data; it is unlikely that the true PSF will be 40% larger than the modelled PSF, and distortions as severe as the $\gamma = 30$ “warp” would require drastic mis-calibration.

4.2.3. Deconvolving real astronomical data

In practise, POLISH will be trained offline on simulated data and then applied to real data in quasi-real time. We show that POLISH can reliably deconvolve real observations, having only been trained on simulations. To demonstrate this, real astronomical observations (Hallinan et al. 2017) were obtained from the VLA, a Y-shaped, 27-telescope interferometer in New Mexico. Reconstructing the sky from VLA data is a more challenging problem than what we will be faced with at DSA-2000, as it has far fewer telescopes and therefore a much more degraded PSF (Figure 4). Evidenced by the strong artifacts in the dirty image of Fig. 8, the VLA’s PSF is much less suppressed off-axis than that of DSA-2000. The PSF is also highly azimuthally asymmetric due to the Y-shape of the array, leading to six radial “struts” expanding outwards from each source in the dirty image.

In Fig. 8 we demonstrate that POLISH can deconvolve the real VLA dirty image, leaving behind fewer imaging artifacts than the traditional image-plane CLEAN algorithm. Fig. 8 shows a comparison of the dirty (input) image, POLISH reconstruction, and CLEAN reconstruction (left to right) for a 0.1×0.1 deg region of the 0.4×0.4 deg full image, including a further zoom in on particularly bright radio galaxies (bottom row). The difference between CLEAN and POLISH for the bright galaxies is striking. CLEAN leaves behind residual structures from the PSF, whereas POLISH produces shapes like those expected for distant radio galaxies.

This result is very promising for two reasons. First, we have shown that a relatively simple simulated data set can train a neural network that will deconvolve real radio interferometric data. Second, the VLA’s sampling of the Fourier plane is much less complete than that of DSA-2000. The fact that POLISH can still perform under these circumstances shows that deep learning based techniques are not only a promising solution for the DSA-2000, but also for other current and future radio interferometers (Jonas & MeerKAT Team 2016; Hotan et al. 2021; Dewdney et al. 2009).

5. RADIO WEAK LENSING & DSA-2000

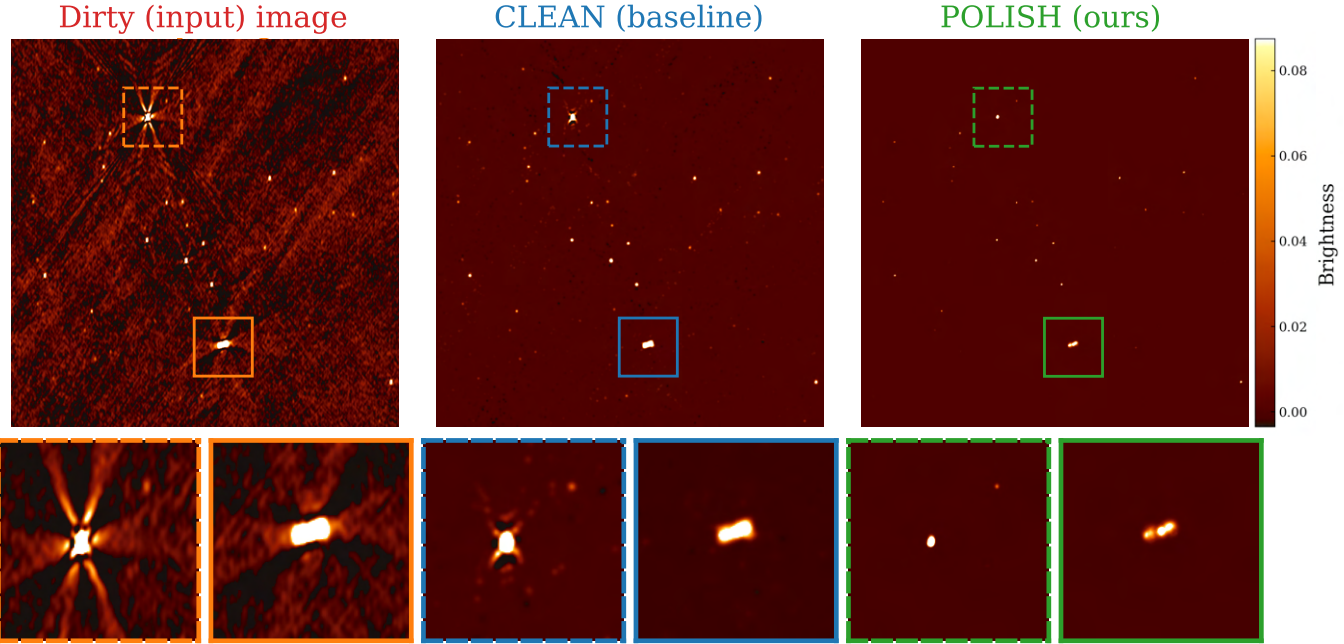


Figure 8. An example of POLISH being applied to real astronomical data from the Very Large Array (VLA), having been trained only on simulated data. The left panel shows the “dirty image” as measured by the VLA, and the right two panels show our neural network (right) and the traditional CLEAN algorithm’s (middle) respective deconvolved reconstructions. We encourage the reader to inspect the high resolution figures in the Supplementary Material.

Weak gravitational lensing is a powerful probe of the Universe’s composition and expansion history, and is an essential tool for constraining the physical nature of dark energy (Kaiser 1998; Hoekstra & Jain 2008; Mandelbaum 2018). Weak lensing imparts a distortion on distant galaxy shapes known as “shear”, causing a separation-dependent correlation between galaxy shapes that is determined by the Universe’s large scale structure and its evolution with time. Measuring the power spectrum of this cosmic shear allows us to constrain the cosmological parameters. To date, weak lensing research has been significantly more advanced at optical wavelengths. However, the achromaticity of gravitational lensing means the large scale structure will imprint itself the same way across the electromagnetic spectrum, while the systematics across wavelengths will vary. Observations in different bands are therefore highly complementary. For a detailed treatment of radio weak lensing in the context of the Square Kilometer Array (SKA) see (Brown et al. 2015; Harrison et al. 2016; Bonaldi et al. 2016; Camera et al. 2017).

In the radio, few surveys thus far have had sufficient angular resolution, sensitivity, and sky coverage to detect the large numbers of SFGs required to do weak lensing cosmology. Using $\sim 9 \times 10^5$ sources in the FIRST survey at 1.4 GHz, Chang et al. (2004) fit galaxies in UV space to make the first-ever radio detection of weak lensing. Demetroullas & Brown (2016) cross-correlated an optical shear map containing ~ 9 million galaxies in the Sloan Digital Sky Survey (SDSS) with a radio shear map from FIRST, resulting in a 2.7σ detection of weak lensing. More recently, the SuperCLASS survey used 0.26 deg^2 of radio data from eMERLIN and the VLA, as well as 1.53 deg^2 of optical data from the Subaru telescope, but had too few sources to make a detection (Harrison et al. 2020). Despite the required catch-up at long wavelengths, there are benefits to doing weak lensing in the radio. For example, the PSF of a radio interferometer can be known a priori, which is not true for optical telescopes. Furthermore, as both optical and radio lensing experiments will likely be systematics limited, cross-correlation provides a robust and unbiased estimator of the shear powerspectrum (Camera et al. 2017; Harrison et al. 2020). And finally, sensitive radio telescopes such as DSA-2000 and the SKA are expected to probe higher redshifts than comparable optical surveys, with a fatter tail at high z .

The DSA-2000 will survey the whole sky north of declination -30° between 0.7 and 2.0 GHz down to a root-mean square (RMS) noise of just $0.5 \mu\text{Jy}$. The survey will contain approximately 10^9 sources, primarily star forming radio galaxies. This is over one thousand times more galaxies than the FIRST sample where a radio weak lensing signal was first detected (Chang et al. 2004), and with a much cleaner PSF than the VLA (see Fig. 4). However, with a point spread function (PSF) whose full-width at half maximum (FWHM) is roughly $3''$, many radio galaxies will be unresolved

for the DSA-2000 in the dirty image. Using POLISH to achieve super-resolution, DSA-2000 could be competitive and complementary with Stage IV weak lensing experiments such as Euclid and the Vera C. Rubin Observatory. Shear maps from DSA-2000 will therefore enable a symbioses between wavelengths, where cross-correlating radio/optical shear maps allow for tight constraints on both dark energy and modified gravity (Harrison et al. 2016).

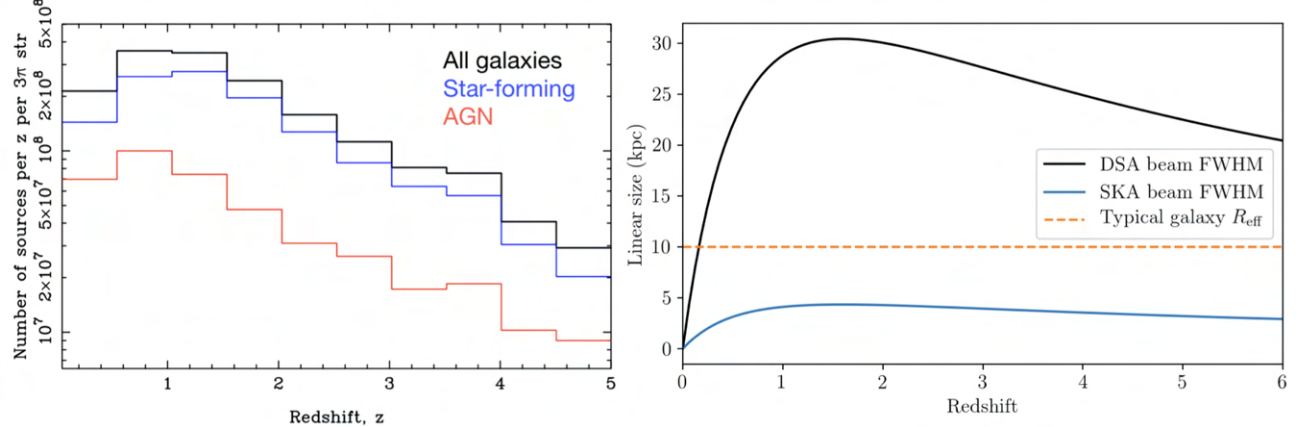


Figure 9. placeholder fig: Can Vikram try and recreate the right panel DSA-2000 will detect an enormous number of star forming galaxies. These can be used for weak lensing cosmology if resolution below the telescope’s PSF width can be achieved. The super-resolution required is roughly a factor of 2–3, as can be seen in the ratio of the black to orange curves in the right panel.

5.1. Radio weak lensing systematics

Shape noise on the shear powerspectrum falls in proportion to the number of galaxies in the survey. But systematic uncertainties will play a large role in upcoming weak lensing surveys, whether in the radio or optical. For example, the intrinsic alignment of galaxies can break the assumption that galaxy position angles and shapes are inherently uncorrelated. Biases in the measurement of shear must be accounted for and carefully calibrated out, as well as uncertainty in redshift estimation (Mandelbaum 2018). Finally, the PSF must be deconvolved out of the image, and residual PSF errors will lead to galaxy shape distortions. In the case of ground-based optical telescopes, time-variable seeing and related systematics make PSF modelling a central effort in weak lensing analysis (Gatti et al. 2021; Jarvis et al. 2021).

In the radio, weak lensing experiments suffer from overlapping but distinct systematics. Intrinsic alignment bias will affect galaxies in any weak lensing survey, but can potentially be calibrated out in the radio using the polarized emission of star forming galaxies, which is unaltered by lensing (Brown & Battye 2011; Harrison et al. 2016). The PSF of a radio interferometer can be modelled deterministically (see Section 2.1), in contrast to an optical telescope. But PSF modelling is still a source of significant uncertainty because the PSF of an interferometer is typically poorly behaved, with significant sidelobes and azimuthal structure thanks to sparse sampling of the aperture. This makes image reconstruction, and therefore shear measurement, more sensitive to errors in the PSF model even if the response can be forward modelled.

The DSA-2000 will skirt some of these issues by densely sampling the UV plane and by optimizing antenna configuration to produce an azimuthally smooth PSF and highly attenuated sidelobes. While its suppressed sidelobes and smoothness will reduce errors introduced by PSF modelling and deconvolution, the nominal beam size of $3''$ means that many SFGs will have angular size below our diffraction limit, hence our requirement of super-resolution. The DSA-2000 will therefore have fewer image reconstruction relics that bias galaxy shape measurement, but will have to infer shear from a small number of pixels, even with POLISH. For reference, the Dark Energy Survey has a median seeing of roughly $1''$ and has produced strong cosmological constraints from its weak lensing experiment (Gatti et al. 2021).

5.2. Forecasting

We would like to estimate how well a weak-lensing survey on DSA-2000 will be able to constrain the cosmological parameters, both in the case where super-resolution of a factor of a few is achieved (POLISH SR in Table 5.2) and

Survey	N_{gal}	Sky coverage (deg 2)	n_{gal} (sq arcmin $^{-1}$)	f_z	σ_{pz}
DSA-2000: POLISH SR	10^9	32,000	6/3 †	0.15	0.05
DSA-2000: No SR	10^9	32,000	6/0.5 †	0.15	0.05
SKA1	5×10^7	5,000	2.7	0.15	0.05
Euclid	1.6×10^9	15,000	30	0.33	0.04
DES Y3	10^8	4,143	6.7/5.6 †	0.0	0.05

Table 1. Parameters used for forecasting the constraining power of a weak lensing experiment on different surveys, including DSA-2000 with and without POLISH’s super-resolution. N_{gal} is the total number of detections, n_{gal} is the on-sky density, f_z is the fraction of galaxies with spectroscopic redshift, and σ_{pz} is the uncertainty on photometric redshifts. The DES Y3 row corresponds to the real values obtained from the year 3 galaxy shape catalog (Gatti et al. 2021); the other rows are estimates of survey parameters.

\dagger Effective aerial number density of galaxies. On DSA-2000 we assume that only half of galaxies will be sufficiently super-resolved to produce a shape measurement.

when spatial resolution is limited by the synthesised beam size of 3” (No SR in Table 5.2). We compare simulations for DSA-2000 with simulations of SKA1 and the Euclid. Euclid is a visible to near-infrared space telescope expected to launch in mid- to late-2022 and is considered a Stage IV experiment. For these forecasts we use the same parameters assumed by Harrison et al. (2016). SKA1 will be a mixed array of 133 15 m SKA dishes and 64 13.5 m dishes from the MeerKAT telescope⁵ and a nominal PSF of 0.5”. Its weak lensing survey will be on Band 2 at 0.95–1.76 GHz (Harrison et al. 2016). As an empirical benchmark, we take the recently-published Dark Energy Survey (DES) Year 3 Results (DES Collaboration et al. 2021). DES is a Stage III experiment that is already producing cosmological strong constraints from its optical weak lensing survey. We show these survey parameters in Table 5.2. We base our estimate of the effective number of usable galaxies on both the estimated PSF sizes and the observed distribution of galaxy sizes. Owen & Morrison (2008) find that half of SFGs above 15 μ Jy have major-axes greater than 1”. From our radio sky simulations and previous work (Bonaldi et al. 2016), we find that only 10% of sources are larger than 3”. For this reason we assume that a weak lensing survey on DSA-2000 with POLISH will have an effective areal density of 3 galaxies per square arcminute, while only 0.5 galaxies per square arcminute will be possible without super-resolution. We assume that SKA1 will be able to resolve $\mathcal{O}(1)$ of detected galaxies, so we do not adjust its n_{gal} . The same is true for Euclid, which is space-based and therefore diffraction limited at its nominal resolution of 0.2”.

Forecasting weak lensing constraints requires each survey’s expected redshift distribution, areal density of galaxies, n_{gal} , total sky coverage, and information about the error in lensed galaxy redshifts. Obtaining redshifts of the lensed galaxies is an important component of weak lensing, as the cross-correlation angular powerspectra between different redshift bins offers information on the evolution of structure over cosmic time (Bonnett et al. 2016). For this analysis, we follow Harrison et al. (2016) in using the MCMC parameter estimation code CosmoSIS (Zuntz et al. 2015). Specifically, we use code they have developed for forecasting the SKA’s radio weak lensing survey⁶, but with the putative DSA-2000 parameters (Hallinan et al. 2021). On DSA-2000, XX% of source will have spectroscopic redshifts (i.e. zero redshift uncertainty). The error on photometric redshifts will be approximately 0.05. DSA-2000 will obtain galaxy redshifts using several different methods. Approximately 30 million galaxies at $z < 1$ will have spectroscopic redshifts from the DSA’s HI survey. The SPHEREx near-infrared all-sky survey will determine the redshifts of three hundred million galaxies with $\sigma_z/(1+z) \leq 10\%$ (Doré et al. 2014), of which three quarters can be cross-matched with the DSA-2000 catalog.

We focus here on DSA-2000’s ability to constrain the matter density and matter power spectrum normalization, Ω_m and σ_8 respectively, as well as the dark energy equation of state parameters w and w_a . In Figure 10 we show the cosmological parameter posteriors produced by CosmoSIS for DSA-2000, Euclid, and SKA1. The red regions show the 1- and 2- σ constraints from DES Y3 results. We use their three two-point (3x2pt) correlation functions in cosmic shear, galaxy clustering, and shear with lens galaxy positions (DES Collaboration et al. 2021). We find that SKA1’s weak lensing survey will be comparable to the DES 3x2pt constraints in constraining both the matter powerspectrum and dark energy. DSA-2000 produces constraints that are nearly as tight as Euclid. All four surveys provide an excellent

⁵ https://www.skatelescope.org/wp-content/uploads/2021/02/22380_SKA_Project-Summary_v4_single-pages.pdf

⁶ <https://bitbucket.org/joezuntz/cosmosis-ska-forecasting/src/master/>

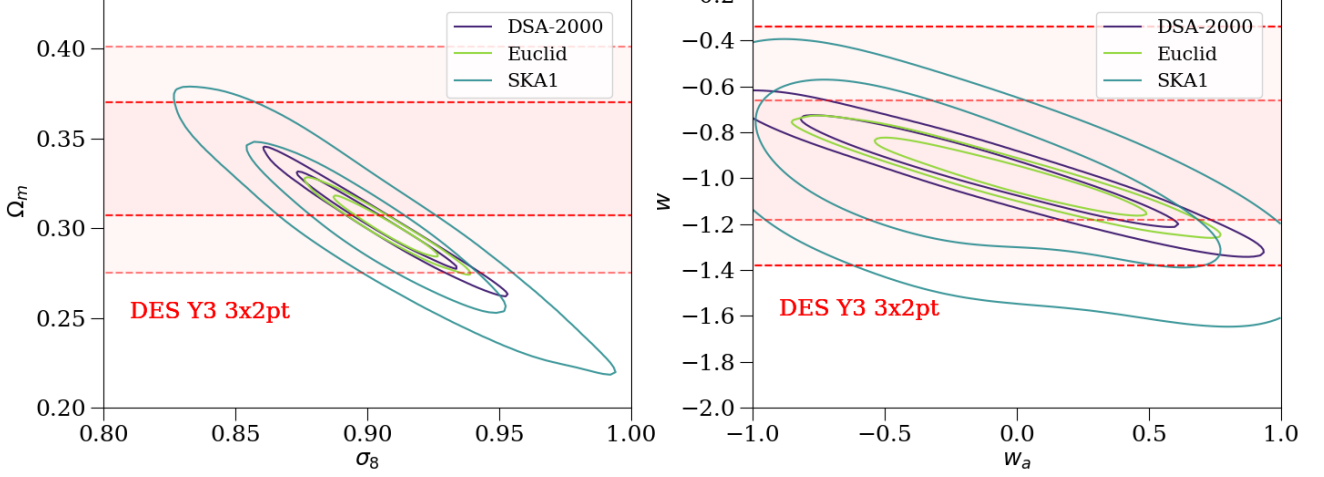


Figure 10. Marginalized constraints on dark energy equation of state parameters, w and w_a (left), and matter powerspectrum parameters, Ω_m and σ_8 (right) for weak lensing surveys on DSA-2000 (with super-resolution), Euclid, and SKA1. The red shaded regions are the 1- and 2- σ constraints from the Dark Energy Survey Year 3 (DES Y3 3x2pt) data after combining three two-point correlation functions (cosmic shear, galaxy clustering, and shear with lens galaxy positions) (DES Collaboration et al. 2021). Note that the forecasts for DSA-2000, Euclid, and SKA1 are cosmic shear only, but do not include lensing systematics.

op:
20:

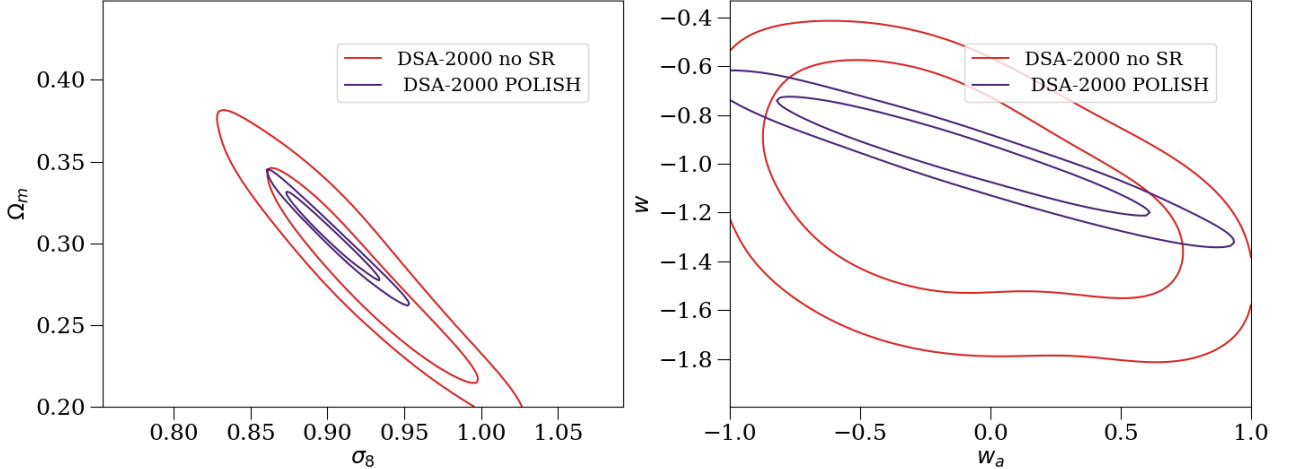


Figure 11. Comparing the ability of weak lensing survey on DSA-2000 to constrain the cosmological parameters with (purple) and without (red) super-resolution.

6. DISCUSSION & CONCLUSION

We have developed and demonstrated POLISH: a high dynamic range residual neural network for fast, accurate and super-resolved astronomical imaging with radio interferometers. Feed forward approaches like POLISH will be essential in analyzing data from upcoming instruments with enormous data rates where stream processing is critical, such as the upcoming DSA-2000 (Hallinan et al. 2021). We have shown that POLISH is highly effective at deconvolving the PSF in both simulated and real astronomical data. It also achieves super-resolution and outperforms the interferometric deconvolution algorithm of the last five decades, image-plane CLEAN, in both reconstruction accuracy (PSNR and SSIM) and resolution. We have shown how method forward-modelling approaches such as RML are not a viable option for surveys such as DSA-2000, where data rates preclude the preservation of visibilities. In its current form, POLISH

(like CLEAN) does not provide errors for its output image. Looking forward, we plan to estimate uncertainty in the reconstructed image within the POLISH framework using Bayesian deep learning to produce a posterior for \hat{I}_{sky} .

Besides addressing the deconvolution problem in radio-interferometric images, POLISH makes possible new, currently inaccessible science by achieving super-resolution. When applied to data from the DSA-2000, POLISH will allow accurate shape measurements of $\sim 10^9$ galaxies, enabling a weak lensing survey. We have forecasted the DSA-2000's ability to constrain cosmological parameters and compared it with both upcoming and current weak lensing experiments. POLISH also delivers higher dynamic range in the vicinity of bright radio sources, which will be important for the discovery of the faint afterglows to the mergers of neutron stars discovered through their gravitational-wave emission, a key target for the DSA-2000 (Hallinan et al. 2017). We anticipate that techniques such as POLISH that deliver robust deconvolution and super-resolution in large data sets will transform the study of the Universe with radio interferometers.

ACKNOWLEDGEMENTS

We thank Martin Krasser for his Tensorflow 2.x implementation of several super-resolution algorithms and his advice on this paper's application. We thank Joe Zuntz for help with his CosmoSIS code. We also thank Nitika Yadlapalli, Yuping Huang, and Ian Harrison for helpful discussion.

APPENDIX

A. RADIO SKY SIMULATION

DSA-2000 is expected to detect more than 10^9 distinct radio sources over the entire sky above -30° (Hallinan et al. 2021). Its 2000×5 m dishes and ultra low noise electronics will allow for 500 nJy per beam rms noise, meaning the majority of those sources will be star forming radio galaxies (Mancuso et al. 2017). For this reason, and because we are focused here on the weak lensing of such objects, our nominal simulation includes only SFRGs. We assume a projected density of galaxies, in this case approximately 6 per square arcminute, multiply it by the image size solid angle, and draw from a Poisson distribution with that value as its mean to get the number of sources to simulate. For now, we include no spatial correlation between the galaxies. Each is taken to be an ellipsoid with Gaussian fall-off.

As a diffuse background, we use the Global Sky Model (GSM) (Price 2016; Zheng et al. 2017). To generate random patches of background emission for each simulated true sky image, we randomly scramble the phases of the spherical harmonic transformed map with the Galaxy masked. We then discard larger scales than those to which DSA-2000 will be sensitive and project back into the image plane.

Galaxy ellipticity is drawn from a beta distribution, which is bounded on the interval [0,1]. We choose shape parameters $\alpha = 1.7$ and $\beta = 4.5$, matching an analytic fit to VLA-COSMOS galaxy shapes (Tunbridge et al. 2016). The source counts distribution is taken to be a broken power-law with a turnover from Euclidean ($N(> F) \propto F^{-3/2}$) to a flatter distribution at XX mJy citeXX. The SFRG size distribution is taken from citexx, which we model as a Gamma distribution in semi-major axis with shape parameters 2.25 and 1.5. Based on DSA-2000's projected sensitivity, we use a source density of 6 per square arcminute. Finally, we model the spectral index of each source as a Gaussian distribution centered on -0.55 and with standard deviation 0.25, based on the known spectral properties of such galaxies at 0.7–2 GHz (Tisanić et al. 2019).

REFERENCES

- Abdulaziz, A., Dabbech, A., & Wiaux, Y. 2019, MNRAS, 489, 1230, doi: [10.1093/mnras/stz2117](https://doi.org/10.1093/mnras/stz2117)
- Akiyama, K., Alberdi, A., Alef, W., et al. 2019, The Astrophysical Journal Letters, 875, L4
- Bertin, E., & Arnouts, S. 1996, A&AS, 117, 393, doi: [10.1051/aas:1996164](https://doi.org/10.1051/aas:1996164)
- Bonaldi, A., Harrison, I., Camera, S., & Brown, M. L. 2016, MNRAS, 463, 3686, doi: [10.1093/mnras/stw2104](https://doi.org/10.1093/mnras/stw2104)
- Bonaldi, A., An, T., Brüggen, M., et al. 2021, MNRAS, 500, 3821, doi: [10.1093/mnras/staa3023](https://doi.org/10.1093/mnras/staa3023)
- Bonnett, C., Troxel, M. A., Hartley, W., et al. 2016, PhRvD, 94, 042005, doi: [10.1103/PhysRevD.94.042005](https://doi.org/10.1103/PhysRevD.94.042005)
- Bouman, K. L., Johnson, M. D., Zoran, D., et al. 2016, in The IEEE Conference on Computer Vision and Pattern Recognition (CVPR), 913. <https://arxiv.org/abs/1512.01413>

- Brown, M., Bacon, D., Camera, S., et al. 2015, in Advancing Astrophysics with the Square Kilometre Array (AASKA14), 23. <https://arxiv.org/abs/1501.03828>
- Brown, M. L., & Batty, R. A. 2011, MNRAS, 410, 2057, doi: [10.1111/j.1365-2966.2010.17583.x](https://doi.org/10.1111/j.1365-2966.2010.17583.x)
- Camera, S., Harrison, I., Bonaldi, A., & Brown, M. L. 2017, MNRAS, 464, 4747, doi: [10.1093/mnras/stw2688](https://doi.org/10.1093/mnras/stw2688)
- Chang, T.-C., Refregier, A., & Helfand, D. J. 2004, ApJ, 617, 794, doi: [10.1086/425491](https://doi.org/10.1086/425491)
- Clark, B. G. 1980, A&A, 89, 377
- Demetroullas, C., & Brown, M. L. 2016, MNRAS, 456, 3100, doi: [10.1093/mnras/stv2876](https://doi.org/10.1093/mnras/stv2876)
- DES Collaboration, Abbott, T. M. C., Aguena, M., et al. 2021, arXiv e-prints, arXiv:2105.13549. <https://arxiv.org/abs/2105.13549>
- Dewdney, P. E., Hall, P. J., Schilizzi, R. T., & Lazio, T. J. L. W. 2009, IEEE Proceedings, 97, 1482, doi: [10.1109/JPROC.2009.2021005](https://doi.org/10.1109/JPROC.2009.2021005)
- Dong, C., Loy, C. C., He, K., & Tang, X. 2015, IEEE transactions on pattern analysis and machine intelligence, 38, 295
- Doré, O., Bock, J., Ashby, M., et al. 2014, arXiv e-prints, arXiv:1412.4872. <https://arxiv.org/abs/1412.4872>
- Event Horizon Telescope Collaboration, Akiyama, K., Alberdi, A., et al. 2019, ApJL, 875, L1, doi: [10.3847/2041-8213/ab0ec7](https://doi.org/10.3847/2041-8213/ab0ec7)
- Gatti, M., Sheldon, E., Amon, A., et al. 2021, MNRAS, 504, 4312, doi: [10.1093/mnras/stab918](https://doi.org/10.1093/mnras/stab918)
- Gatti, M., Sheldon, E., Amon, A., et al. 2021, Monthly Notices of the Royal Astronomical Society, 504, 4312, doi: [10.1093/mnras/stab918](https://doi.org/10.1093/mnras/stab918)
- Glasner, D., Bagon, S., & Irani, M. 2009, in 2009 IEEE 12th international conference on computer vision, IEEE, 349–356
- Hallinan, G., Ravi, V., & Deep Synoptic Array Team. 2021, in American Astronomical Society Meeting Abstracts, Vol. 53, American Astronomical Society Meeting Abstracts, 316.05
- Hallinan, G., Corsi, A., Mooley, K. P., et al. 2017, Science, 358, 1579, doi: [10.1126/science.aap9855](https://doi.org/10.1126/science.aap9855)
- Harrison, I., Camera, S., Zuntz, J., & Brown, M. L. 2016, MNRAS, 463, 3674, doi: [10.1093/mnras/stw2082](https://doi.org/10.1093/mnras/stw2082)
- Harrison, I., Brown, M. L., Tunbridge, B., et al. 2020, MNRAS, 495, 1737, doi: [10.1093/mnras/staa696](https://doi.org/10.1093/mnras/staa696)
- Hoekstra, H., & Jain, B. 2008, Annual Review of Nuclear and Particle Science, 58, 99, doi: [10.1146/annurev.nucl.58.110707.171151](https://doi.org/10.1146/annurev.nucl.58.110707.171151)
- Högbom, J. A. 1974, A&AS, 15, 417
- Hotan, A. W., Bunton, J. D., Chippendale, A. P., et al. 2021, PASA, 38, e009, doi: [10.1017/pasa.2021.1](https://doi.org/10.1017/pasa.2021.1)
- Jarvis, M., Bernstein, G. M., Amon, A., et al. 2021, MNRAS, 501, 1282, doi: [10.1093/mnras/staa3679](https://doi.org/10.1093/mnras/staa3679)
- Jonas, J., & MeerKAT Team. 2016, in MeerKAT Science: On the Pathway to the SKA, 1
- Kaiser, N. 1998, The Astrophysical Journal, 498, 26
- Ledig, C., Theis, L., Huszár, F., et al. 2017, in Proceedings of the IEEE conference on computer vision and pattern recognition, 4681–4690
- Lim, B., Son, S., Kim, H., Nah, S., & Mu Lee, K. 2017, in Proceedings of the IEEE Conference on Computer Vision and Pattern Recognition (CVPR) Workshops
- Mancuso, C., Lapi, A., Prandoni, I., et al. 2017, ApJ, 842, 95, doi: [10.3847/1538-4357/aa745d](https://doi.org/10.3847/1538-4357/aa745d)
- Mandelbaum, R. 2018, Annual Review of Astronomy and Astrophysics, 56, 393
- McMullin, J. P., Waters, B., Schiebel, D., Young, W., & Golap, K. 2007, in Astronomical Society of the Pacific Conference Series, Vol. 376, Astronomical Data Analysis Software and Systems XVI, ed. R. A. Shaw, F. Hill, & D. J. Bell, 127
- Narayan, R., & Nityananda, R. 1986, ARA&A, 24, 127, doi: [10.1146/annurev.aa.24.090186.001015](https://doi.org/10.1146/annurev.aa.24.090186.001015)
- Offringa, A. R., McKinley, B., Hurley-Walker, N., et al. 2014, MNRAS, 444, 606, doi: [10.1093/mnras/stu1368](https://doi.org/10.1093/mnras/stu1368)
- Owen, F. N., & Morrison, G. E. 2008, AJ, 136, 1889, doi: [10.1088/0004-6256/136/5/1889](https://doi.org/10.1088/0004-6256/136/5/1889)
- Pratley, L., McEwen, J. D., d'Avezac, M., et al. 2018, MNRAS, 473, 1038, doi: [10.1093/mnras/stx2237](https://doi.org/10.1093/mnras/stx2237)
- Price, D. C. 2016, PyGSM: Python interface to the Global Sky Model. <http://ascl.net/1603.013>
- Ravi, V., Catha, M., D'Addario, L., et al. 2019, Nature, 572, 352, doi: [10.1038/s41586-019-1389-7](https://doi.org/10.1038/s41586-019-1389-7)
- Riad, S. 1986, Proceedings of the IEEE, 74, 82, doi: [10.1109/PROC.1986.13407](https://doi.org/10.1109/PROC.1986.13407)
- Shi, W., Caballero, J., Huszar, F., et al. 2016, in Proceedings of the IEEE Conference on Computer Vision and Pattern Recognition (CVPR)
- Starck, J. L., Pantin, E., & Murtagh, F. 2002, Publications of the Astronomical Society of the Pacific, 114, 1051, doi: [10.1086/342606](https://doi.org/10.1086/342606)
- Sun, H., & Bouman, K. L. 2020, arXiv e-prints, arXiv:2010.14462. <https://arxiv.org/abs/2010.14462>
- Tisanić, K., Smolčić, V., Delhaize, J., et al. 2019, A&A, 621, A139, doi: [10.1051/0004-6361/201834002](https://doi.org/10.1051/0004-6361/201834002)
- Tunbridge, B., Harrison, I., & Brown, M. L. 2016, MNRAS, 463, 3339, doi: [10.1093/mnras/stw2224](https://doi.org/10.1093/mnras/stw2224)
- Wang, Z., Bovik, A. C., Sheikh, H. R., & Simoncelli, E. P. 2004, IEEE Transactions on Image Processing, 13, 600, doi: [10.1109/TIP.2003.819861](https://doi.org/10.1109/TIP.2003.819861)

- Wiaux, Y., Jacques, L., Puy, G., Scaife, A. M. M., & Vanderghenst, P. 2009, MNRAS, 395, 1733,
doi: [10.1111/j.1365-2966.2009.14665.x](https://doi.org/10.1111/j.1365-2966.2009.14665.x)
- Xu, L., Ren, J. S., Liu, C., & Jia, J. 2014, Advances in neural information processing systems, 27, 1790
- Yan, R., & Shao, L. 2016, IEEE Transactions on Image Processing, 25, 1910, doi: [10.1109/TIP.2016.2535273](https://doi.org/10.1109/TIP.2016.2535273)
- Yang, C.-Y., Ma, C., & Yang, M.-H. 2014, in European conference on computer vision, Springer, 372–386
- Yang, W., Zhang, X., Tian, Y., et al. 2019, IEEE Transactions on Multimedia, 21, 3106,
doi: [10.1109/TMM.2019.2919431](https://doi.org/10.1109/TMM.2019.2919431)
- Yu, J., Fan, Y., Yang, J., et al. 2018, arXiv preprint arXiv:1808.08718
- Zheng, H., Tegmark, M., Dillon, J. S., et al. 2017, MNRAS, 464, 3486, doi: [10.1093/mnras/stw2525](https://doi.org/10.1093/mnras/stw2525)
- Zuntz, J., Paterno, M., Jennings, E., et al. 2015, Astronomy and Computing, 12, 45, doi: [10.1016/j.ascom.2015.05.005](https://doi.org/10.1016/j.ascom.2015.05.005)